applied optics

Spectral response of large-area luminescent solar concentrators

Yilin Li,[1,*] Yongcao Zhang,[2] Yujian Sun,[3] and Tianhui Ren[4]

[1]Department of Chemical and Biomolecular Engineering, Rice University, Houston, Texas 77005, USA
[2]Department of Mechanical Engineering, University of Houston, Houston, Texas 77004, USA
[3]School of Environmental and Forest Sciences, University of Washington, Seattle, Washington 98195, USA
[4]School of Chemistry and Chemical Engineering, Shanghai Jiao Tong University, Shanghai, 200240, China
*Corresponding author: yilinli@rice.edu

Received 21 July 2020; revised 9 September 2020; accepted 12 September 2020; posted 14 September 2020 (Doc. ID 403354); published 1 October 2020

Measuring the spectral response (SR) of large-area (>100 cm^2) luminescent solar concentrators (LSCs) has proven difficult because common laboratory photovoltaic (PV) instruments that offer monochromatic incidence measure devices with limited sizes (typically <50 cm^2). This report addresses this issue through a method called regional measurements. In this method, large-area LSCs are configured to small surface and edge regions, which are sequentially illuminated and measured, respectively. The measured SRs of large-area LSCs are consistent with those from the conventional method and the Monte Carlo ray-tracing simulation. This method is also applied to analyze scattering effects in the LSCs, showing the relationships of the scattering-induced power gain and power loss to the surface root-mean-squared roughness (R_q) of the devices. The results explain why the PV performance of the LSCs can be improved through proper surface scattering treatment.

https://doi.org/10.1364/AO.403354

1. INTRODUCTION

The integration of photovoltaic (PV) devices with buildings in the built environment has been attracted a lot of attention in recent years [1–3]. Luminescent solar concentrators (LSCs) are one of the promising building-integrated PV technologies because they offer visual comfort to human beings when harvesting solar energy [4–6]. As shown in Fig. 1, LSCs are typically planar optical PV devices consisting of luminophore-doped waveguides (i.e., luminescent waveguides) with solar cells attached to the edges [7–9]. In the operational mechanism, short-wavelength photons are converted to long-wavelength photons, which are redirected to the solar cells through successive total internal reflection (TIR) in the waveguide [10–13]. This design allows the LSCs to work optimally under direct and diffuse light conditions [14–16]. The colorful appearance also allows the LSCs to impart aesthetics to the buildings in the built environment [17–22].

In the past decades, high-efficiency LSCs have been developed due to the advancements of luminophore synthesis and optical techniques [23–25]. Slooff *et al.* reported an LSC with high efficiency of 7.1% through luminophore energy transfer [23]. Goldschmidt *et al.* designed a tandem device using two layers of LSCs with different luminophores, which achieved an efficiency of 6.7% [24]. Desmet *et al.* improved the efficiency of an LSC from 3.4% to 4.2% using microcellular polyethylene terephthalate (MCPET) back reflectors [25]. In these studies, LSCs are treated as common PV devices, and the PV performance is described as using the standard power conversion efficiency (PCE), which is the maximum electrical energy from the device relative to the incident light energy [26–28]. In studies where only the luminescent waveguides are studied, optical quantum efficiency (OQE) is used instead of PCE, which is the number of emitted photons at the edge of the luminescent waveguide relative to the number of incident photons [29–31]. While these figures of merit are extensively reported, there are a handful of studies reporting the spectral response (SR) of the LSCs [23,32–37] as noted in Table 1. Common laboratory PV instruments measure devices with very limited sizes (<50 cm^2), while typical LSCs have sizes exceeding the measurement limits. Therefore, measuring the SR of the LSCs, especially large-area (>100 cm^2) devices, requires specific PV instruments that provide monochromatic incidence.

In a previous study, we developed a method called regional measurements to analyze large-area (>100 cm^2) LSCs in terms of the PV performance and photon transport mechanism. In this method, LSCs are configured to surface and edge regions, and therefore they can be measured using common PV instruments [38]. In this study, we extend the capability of this method to measure the SR of large-area (>100 cm^2) LSCs. Monochromatic light is used instead of the full-spectrum

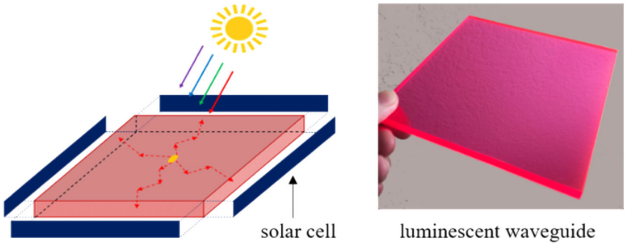

Fig. 1. Concept and operational mechanism of the LSCs.

Table 1. Studies Reporting the SR of the LSCs

Entry	LSC Size	References
1	$5 \times 5\ cm^2$	[23]
2	$5 \times 5\ cm^2$	[32]
3	$4 \times 6\ cm^2$	[33]
4	$7.8 \times 7.8\ cm^2$	[34]
5	$2.5 \times 2.5\ cm^2$	[35]
6	$7 \times 7\ cm^2$	[36]
7	$5 \times 5\ cm^2$	[37]
8	$>10 \times 10\ cm^2$	this work

simulated AM1.5 G sunlight. The results help to understand the scattering effects in the LSCs.

2. EXPERIMENTAL SETUP

LSCs were fabricated according to the literature [39,40]. The thickness of the luminescent waveguides, made of poly(methyl methacrylate) (PMMA) doped with BASF Lumogen Red 305 (R305) (luminophore load: 60 ppm, visible transparency: 24%), is 0.25 in (0.635 cm) [41]. A small polycrystalline silicon (p-Si) solar cell is used in this method, which avoids tedious procedures to cut and connect solar cells for matching the size of the waveguide edge [38]. As illustrated in Fig. 2(a), the experimental setup contains a luminescent waveguide, a mask with a hole to allow the monochromatic incidence on a certain region on the waveguide surface, a solar cell attached to a certain region on the waveguide edge, and black tape to cover rest of the waveguide edge. No backside reflector was used in the measurements. As illustrated in Fig. 2(b), for example, for a $4 \times 4\ in^2$ ($10.16 \times 10.16\ cm^2$) LSC, 16 surface regions are illuminated by monochromatic incidence through a $1 \times 1\ in^2$ ($2.54 \times 2.54\ cm^2$) hole on the mask. For each illuminated surface region, 16 edge regions are measured using the solar cell.

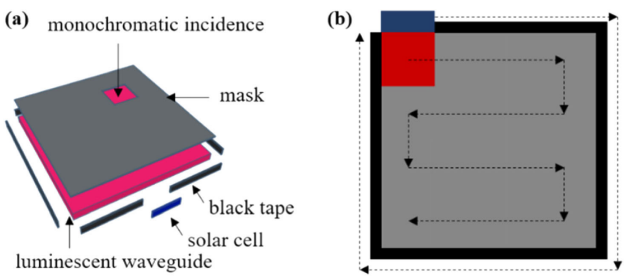

Fig. 2. Experimental (a) setup and (b) procedures to measure the SR of the LSCs.

The SR of the device ($SR(\lambda)$, $A \cdot W^{-1}$), which is the short-circuit current produced by the device (I_{sc}, A) relative to the power of the monochromatic incidence (P_{in}, W), is calculated by Eq. (1):

$$SR(\lambda) = \frac{\sum I_{sc}(\lambda)}{\sum P_{in}(\lambda)}, \tag{1}$$

where $\Sigma I_{sc}(\lambda)$ is the sum of the I_{sc} measured at each edge region, and $\Sigma P_{in}(\lambda)$ is the sum of the P_{in}. $P_{in}(\lambda)$ is measured by a reference solar cell of known $SR(\lambda)$.

In this study, the SR is converted to external quantum efficiency (EQE), which is the most widely reported. It is defined as the number of electrons produced by the device relative to the number of the monochromatic photons and calculated by Eq. (2):

$$EQE(\lambda) = \frac{hc}{q\lambda} SR(\lambda), \tag{2}$$

where h ($m^2 \cdot kg \cdot s^{-1}$) is the Planck constant, c ($m \cdot s^{-1}$) is the speed of light, and q(C) is the elementary charge.

The monochromatic incidence was provided by an OAI class AAA solar simulator coupled with a monochromator. The I_{sc} was measured using a Keithley 2401 source meter. The surface root-mean-squared (RMS) roughness (R_q) was calculated from the height profile of the waveguide, which was measured using a Bruker ICON Atomic Force Microscope (AFM) with noncontact mode.

3. RESULTS AND DISCUSSION

The method of regional measurements is validated by comparing the EQEs with those from the conventional method and the Monte Carlo ray-tracing simulation (MCRTS) on small-area ($<100\ cm^2$) LSCs. In the conventional method, no mask and black tape were used, and the LSCs were treated as common PV devices and measured according to standard procedures [42] to afford PV parameters such as J_{sc} and PCE. MCRTS was developed according to the literature [43–45]. Typical loss mechanisms were considered in the MCRTS, such as incomplete absorption of the incident light, luminophore self-absorption, matrix absorption, internal scattering, and surface scattering [4]. Wavelength-dependent parameters were used in the MCRTS for describing the loss mechanisms.

In this study, we focus on LSCs with sizes of $1 \times 1\ in^2$ ($2.54 \times 2.54\ cm^2$), $2 \times 2\ in^2$ ($5.08 \times 5.08\ cm^2$), and $3 \times 3\ in^2$ ($7.62 \times 7.62\ cm^2$) because they are small-area ($<100\ cm^2$) devices that meet the size requirement of the instrument for the conventional method. As shown in Figs. 3(a)–3(c), the results from the method of regional measurements are consistent with those from the conventional method and the MCRTS. The EQE starts from 360 nm, which is the UV cutoff wavelength of PMMA [8]. The EQE ends at 1200 nm, which is greater than the absorption edge of Si (1100 nm) due to the indirect band gap, heavily doped impurity bands, and temperature effects [15,46]. The strong EQE from 360 to 620 nm represents the absorption of the luminophore [15]. The spectral tail from 620 to 1200 nm suggests the scattering effects of the LSCs for long-wavelength (>600 nm) photons [40]. The scattering effects

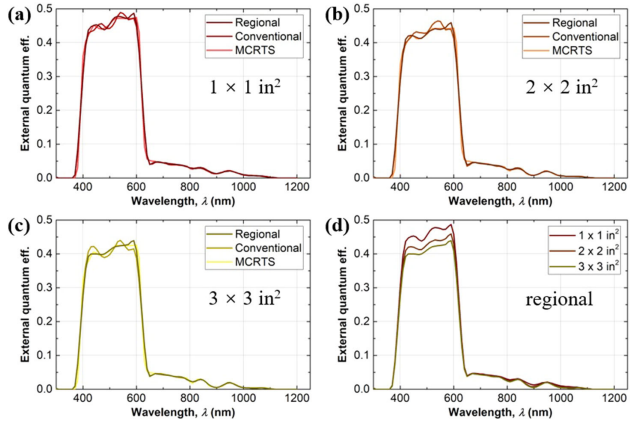

Fig. 3. EQEs of small-area (<100 cm^2) LSCs with sizes of (a) 1 × 1 in^2, (b) 2 × 2 in^2, and (c) 3 × 3 in^2 from the method of regional measurements, the conventional method, and the MCRTS. (d) EQEs from the method of regional measurements.

include internal scattering and surface scattering [4]. The weak scattering effects, indicated by the weak EQE between 620 and 1200 nm, imply a small number of scattering events occurring during the TIR-based photon transport within the waveguide. Figure 3(d) concludes the results for the method of regional measurements with increasing LSC size. The gradual decrease of the EQE in the luminophore absorption range (360–620 nm) is consistent with the decreasing performance of the LSCs due to the increase of the photon transport loss with increasing LSC size. The spectral tails overlap with each other, suggesting that the scattering effects are not affected by the LSC size.

After method validation, we apply this method to measure the SR of large-area (>100 cm^2) LSCs, which have sizes from 4 × 4 in^2 (10.16 × 10.16 cm^2) to 7 × 7 in^2 (17.78 × 17.78 cm^2). Figure 4 demonstrates consistent results from the method of regional measurements and the MCRTS. As expected, the response in the luminophore absorption range (360–620 nm) decreases with increasing LSC size, while the response in the long-wavelength (>600 nm) scattering range (620–1200 nm) is unaffected. This is possibly due to a small geometric gain ($G \leq 7$) of the LSCs in this study, which does not

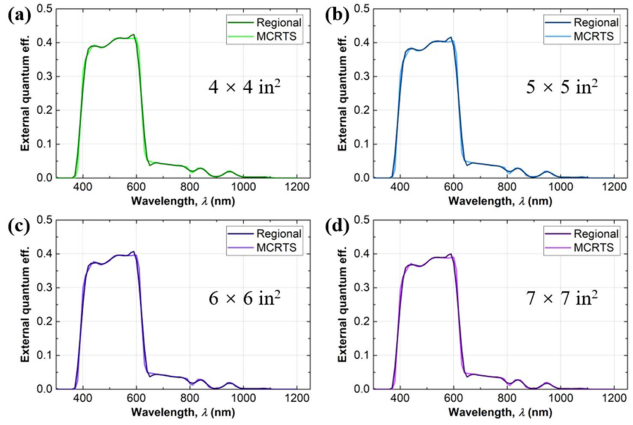

Fig. 4. EQEs of the LSCs with sizes from 4 × 4 in^2 to 7 × 7 in^2 from the method of regional measurements and the MCRTS.

Table 2. Comparison of the J_{sc} with Increasing LSC Size from Different Methods

Size (in^2)	1 × 1	2 × 2	3 × 3	4 × 4	5 × 5	6 × 6	7 × 7
Reg.	52.1	48.3	46.1	44.5	43.4	42.4	41.7
Conv.	51.7	48.5	45.8	n/a	n/a	n/a	n/a
MCRTS	52.0	48.2	46.1	44.7	43.5	42.6	41.8
J-V[a]	51.5	50.0	46.6	45.7	43.2	43.8	41.6

[a]Values are from [15].

lead to an observable change of the scattering effects in the EQE of the LSCs.

The EQEs from the method of regional measurements, the conventional method, and the MCRTS are also integrated with the AM1.5G solar spectrum [$\phi(\lambda)$, $m^{-2} \cdot s^{-1} \cdot nm^{-1}$] to calculate the short-circuit current density (J_{sc}, $A \cdot m^{-2}$) of the LSCs using Eq. (3):

$$J_{sc} = q \int \mathrm{EQE}(\lambda)\phi(\lambda)\mathrm{d}\lambda. \tag{3}$$

Table 2 provides the comparison of the J_{sc} from the method of regional measurements (Reg.), the conventional method (Conv.), the MCRTS, and the J-V curves of the LSCs with varying sizes. The difference in J_{sc} is within 5%, suggestive of consistency among the results. The J_{sc} calculated from the EQE is equivalent to the short-circuit current of the LSCs (four-cell configuration) divided by the area of the top surface of the LSCs [40].

Our final task is to investigate the impact of the scattering effects on the PV performance of the LSCs through the SR measurements. Our recent study shows that proper surface scattering treatment, which adjusts the surface RMS roughness (R_q) of the waveguide, can improve the PCE (obtained from standard J-V measurement) of a 12 × 12 in^2 (30.48 × 30.48 cm^2) LSC by 44% [41]. The surface scattering treatment is applied to the top surface of the waveguide, while the bottom and edge surfaces are kept smooth. Increasing R_q affected the visual performance of the LSCs, leading to the decrease of the surface reflectance and waveguide transmittance but the increase of the haze [41]. As shown in Fig. 5(a), the PCE of the LSC is increased from 1.86% to 2.68% when the R_q is increased from 15 to 63 nm. However, it drops to 2.44% when the R_q is further increased to 105 nm. For blank devices, the PCE gradually increased to its maximum at R_q of 82 nm and then decreased at R_q of 105 nm. The observation of the PCE with increasing R_q can be ascribed to the balance between the scattering-induced power gain and power loss. The scattering-induced power gain primarily comes from the incident light that is not absorbed by the luminophores, which is scattered and directly delivered to the solar cells, while the scattering-induced power loss primarily comes from the scattering-based interruption of the TIR-based luminescent light that is delivered to the solar cells. As depicted in Figs. 5(b)–5(e), the scattering effects, as noticed in the long-wavelength (>600 nm) scattering range (620–1200 nm), are minimal at R_q of 15 nm. With the increase of R_q from 22 to 33 nm and further to 46 nm, the scattering effects gradually increases, while the EQE in the luminophore absorption range (360–620 nm) gradually decreases. The overall effect leads to the performance enhancement for the LSC because

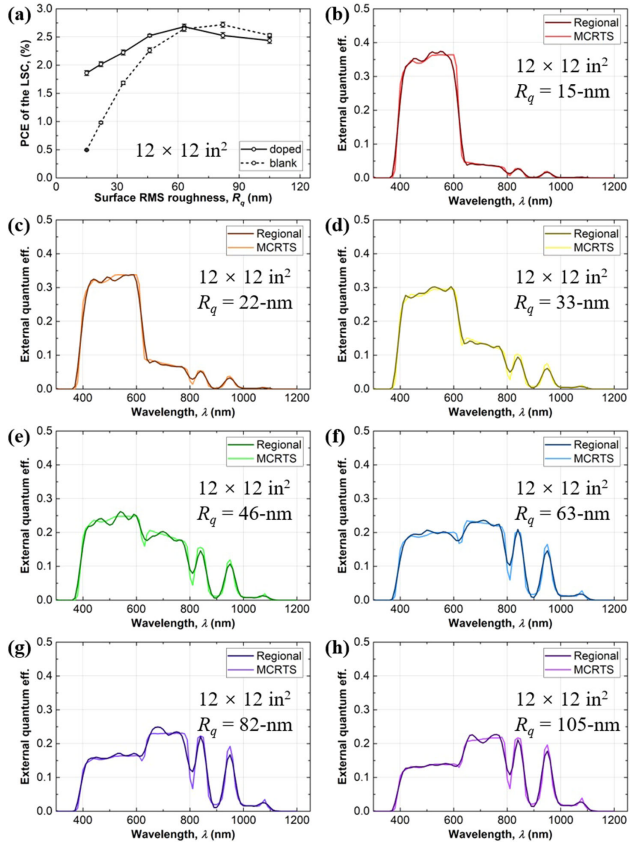

Fig. 5. (a) PCE of a 12 × 12 in² LSC with increasing R_q. (b)–(h) EQEs of a 12 × 12 in² LSC with R_q from 15 to 105 nm from the method of regional measurements and the MCRTS.

the scattering-induced power gain is more than the power loss. At R_q of 63 nm, the scattering-induced power gain surpasses the power loss, and the net gain is maximal. The EQE in Fig. 5(f) covers from 360 to 1200 nm with relatively high values. Therefore, a maximum PCE is achieved. Further increasing the R_q to 82 nm and 105 nm results in more scattering-induced power loss than power gain. As seen in Figs. 5(g) and 5(h), very similar EQEs are obtained for R_q of 82 nm and 105 nm. Our previous study shows that the scattering-induced power gain and power loss depend on the LSC size [41], and therefore the selection of R_q to maximize the PCE is highly dependent on the LSC size. R_q of greater than 63 nm is recommended for small-area (<100 cm²) LSCs, while R_q of less than 63 nm is recommended for super-large- area (>10 m²) devices.

The J_{sc} of the LSCs with varying R_q is calculated using Eq. (3). Table 3 provides a comparison of the J_{sc} from the method of regional measurements (Reg.), the MCRTS, and the J-V curves of the LSCs with varying R_q. The difference in J_{sc} is within 5%, which is a reasonable experimental error due to different experimental setups. The trend of the J_{sc} is consistent with the trend of the PCE in Fig. 5(a), and it maximizes at R_q of 63 nm.

To further understand the mechanism behind the R_q-dependent performance of the LSCs, we performed regional measurement on the 12 × 12 in² (30.48 × 30.48 cm²) LSC with increasing R_q using AM1.5G simulated sunlight according

Table 3. Comparison of the J_{sc} with Varying R_q from Different Methods

R_q (-nm)	15	22	33	46	63	82	105
Reg.	38.7	41.4	46.9	52.3	56.7	56.5	52.9
MCRTS	39.0	41.8	47.3	52.9	56.6	56.3	53.0
J-V[a]	39.9	43.4	48.0	54.9	58.6	55.0	52.9

[a]Values are from [41].

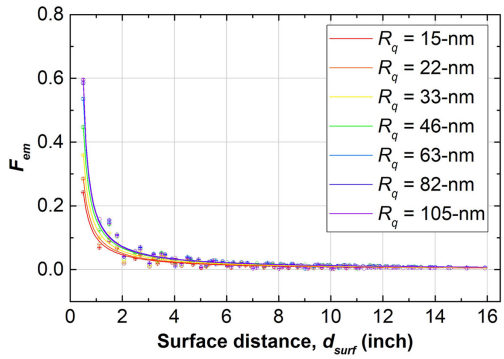

Fig. 6. Relationship between d_{surf} and F_{em} with increasing R_q. Scattered points: measured results. Solid lines: fitting results.

to the literature [38]. One of the key results from the regional measurements is the relationship between d_{surf} and F_{em}. Here d_{surf} (inch) is the surface distance, which is the distance between the illuminated LSC surface region and the measured LSC edge region, and F_{em} represents the number of photons transporting to the LSC edge region relative to the number of photons initially generated and trapped upon the illumination of the LSC surface region. As shown in Fig. 6, the scattering effects exhibit a strong impact on F_{em} when d_{surf} is less than 4 inches (10.16 cm). A high F_{em} is obtained for a smaller d_{surf} and a higher R_q, indicating that more photons transport to the edge of the waveguide. When d_{surf} is greater than 4 inches (10.16 cm), F_{em} becomes close to zero, suggesting a large fraction of photon loss during the photon transport.

A more detailed mechanism can be revealed when the measured results of d_{surf} versus F_{em} were fitted. According to the literature [38], two important parameters, $N_{abs}^{\langle L_{ptn}\rangle_{max}}$ and θ_c, can be obtained from the fitting results. Here $N_{abs}^{\langle L_{ptn}\rangle_{max}}$ is the number of photon absorption (initial absorption + re-absorption) events that occur at the maximum average photon transport distance, and θ_c is the experimental critical angle for the photon surface loss. Table 4 shows that $N_{abs}^{\langle L_{ptn}\rangle_{max}}$ exhibits a decreasing trend with increasing R_q, and it minimizes at R_q of 63 nm, where the 12 × 12 in² (30.48 × 30.48 cm²) LSC exhibits the highest PCE, which signifies that increasing the scattering effects reduces the number of photon absorption/re-absorption events in the waveguide. However, θ_c increases with increasing R_q, suggestive of an increase of surface photon loss. According to the literature [38], θ_c represents the effective critical angle for the surface cone loss. A large θ_c means a large average photon propagation angle. The latter leads to a short optical path length per unit length of d_{surf} and consequently a small $N_{abs}^{\langle L_{ptn}\rangle_{max}}$.

Table 4. Fitting Parameters, $N_{abs}^{\langle L_{ptn}\rangle_{max}}$ and θ_c from the Measured Results of d_{surf} versus F_{em}

R_q (-nm)	15	22	33	46	63	82	105
$N_{abs}^{\langle L_{ptn}\rangle_{max}}$	11.6	10.7	9.5	8.4	7.9	8.0	8.3
θ_c (deg)	38.5	42.5	44.0	44.2	46.3	48.4	50.5

4. CONCLUSIONS

In this paper, we addressed the issue to measure the SR of large-area ($>100\,cm^2$) LSCs, which was not realized in previous studies, using common PV instruments and a small-area solar cell according to a method of regional measurements. In this method, the LSCs were configured to surface and edge regions, which were sequentially illuminated by monochromatic incidence and measured by a solar cell, respectively. The measured SRs, represented by the EQEs, were consistent with those from the conventional method and the MCRTS. The integrated J_{sc} matches well the J_{sc} from the J-V curves. This method was also applied to analyze the scattering effects in a $12 \times 12\,in^2$ ($30.48 \times 30.48\,cm^2$) LSC, showing that high performance can be achieved through proper scattering treatment. The mechanism behind the R_q-dependent performance of the LSCs was further elucidated through the regional measurements using AM1.5G simulated sunlight. A proper surface scattering treatment can reduce the number of photon absorption (initial absorption + re-absorption) events in the waveguide.

Acknowledgment. This work is a part of the project Energy-Harvesting Windows and Panels. The authors would like to thank Solera City Energy for research support.

Disclosures. The authors declare no conflicts of interest.

REFERENCES

1. A. G. Hestnes, "Building integration of solar energy systems," Sol. Energy **67**, 181–187 (1999).
2. R. Baetens, B. P. Jelle, and A. Gustavsen, "Properties, requirements and possibilities of smart windows for dynamic daylight and solar energy control in buildings: a state-of-the-art review," Sol. Energy Mater. Sol. Cells **94**, 87–105 (2010).
3. C. Good, I. Andresen, and A. G. Hestnes, "Solar energy for net zero energy buildings—a comparison between solar thermal, PV and photovoltaic-thermal (PV/T) systems," Sol. Energy **122**, 986–996 (2015).
4. M. G. Debije and P. P. C. Verbunt, "Thirty years of luminescent solar concentrator research: solar energy for the built environment," Adv. Energy Mater. **2**, 12–35 (2012).
5. N. Aste, L. C. Tagliabue, P. Palladino, and D. Testa, "Integration of a luminescent solar concentrator: effects on daylight, correlated color temperature, illuminance level and color rendering index," Sol. Energy **114**, 174–182 (2015).
6. F. Meinardi, F. Bruni, and S. Brovelli, "Luminescent solar concentrators for building-integrated photovoltaics," Nat. Rev. Mater. **2**, 17072 (2017).
7. M. Zettl, O. Mayer, E. Klampaftis, and B. S. Richards, "Investigation of host polymers for luminescent solar concentrators," Energy Technol. **5**, 1037–1044 (2016).
8. Y. Li, X. Zhang, Y. Zhang, R. Dong, and C. K. Luscombe, "Review on the role of polymers in luminescent solar concentrators," J. Polym. Sci. A **57**, 201–215 (2019).
9. G. Griffini, "Host matrix materials for luminescent solar concentrators: recent achievements and forthcoming challenges," Front. Mater. **6**, 29 (2019).
10. W. H. Weber and J. Lambe, "Luminescent greenhouse collector for solar radiation," Appl. Opt. **15**, 2299–2300 (1976).
11. A. Goetzberger and W. Greube, "Solar energy conversion with fluorescent collectors," Appl. Phys. **14**, 123–139 (1977).
12. J. S. Batchelder, A. H. Zewail, and T. Cole, "Luminescent solar concentrators. 1: theory of operation and techniques for performance evaluation," Appl. Opt. **18**, 3090–3110 (1979).
13. J. S. Batchelder, A. H. Zewail, and T. Cole, "Luminescent solar concentrators. 2: experimental and theoretical analysis of their possible efficiencies," Appl. Opt. **20**, 3733–3754 (1981).
14. M. G. Debije and V. A. Rajkumar, "Direct versus indirect illumination of a prototype luminescent solar concentrator," Sol. Energy **122**, 334–340 (2015).
15. Y. Li, Y. Sun, and Y. Zhang, "Luminescent solar concentrators performing under different light conditions," Sol. Energy **188**, 1248–1255 (2019).
16. F. Mateen, M. A. Saeed, J. W. Shim, and S.-K. Hong, "Indoor/outdoor light-harvesting by coupling low-cost organic solar cell with a luminescent solar concentrator," Sol. Energy **207**, 379–387 (2020).
17. W. van Sark, P. Moraitis, C. Aalberts, M. Drent, T. Grasso, Y. L'Ortije, M. Visschers, M. Westra, R. Plas, and W. Planje, "The 'Electric Mondrian' as a luminescent solar concentrator demonstrator case study," Solar RRL **1**, 1600015 (2017).
18. A. Reinders, R. Kishore, L. Slooff, and W. Eggink, "Luminescent solar concentrator photovoltaic designs," Jpn. J. Appl. Phys. **57**, 08RD10 (2018).
19. M. G. Debije, C. Tzikas, M. M. de Jong, M. Kanellis, and L. H. Slooff, "The solar noise barrier project: 3. The effects of seasonal spectral variation, cloud cover and heat distribution on the performance of full-scale luminescent solar concentrator panels," Renew. Energy **116A**, 335–343 (2017).
20. M. G. Debije, C. Tzikas, V. A. Rajkumar, and M. M. de Jong, "The solar noise barrier project: 2. The effect of street art on performance of a large scale luminescent solar concentrator prototype," Renew. Energy **113**, 1288–1292 (2017).
21. M. Kanellis, M. M. de Jong, L. Slooff, and M. G. Debije, "The solar noise barrier project: 1. Effect of incident light orientation on the performance of a large-scale luminescent solar concentrator noise barrier," Renew. Energy **103**, 647–652 (2017).
22. Á. Bognár, S. Kusnadi, L. H. Slooff, C. Tzikas, R. C. G. M. Loonen, M. M. de Jong, J. L. M. Hensen, and M. G. Debije, "The solar noise barrier project 4: modeling of full-scale luminescent solar concentrator noise barrier panels," Renew. Energy **151**, 1141–1149 (2020).
23. L. H. Slooff, E. E. Bende, A. R. Burgers, T. Budel, M. Pravettoni, R. P. Kenny, E. D. Dunlop, and A. Büchtemann, "A luminescent solar concentrator with 7.1% power conversion efficiency," Phys. Status Solidi RRL **2**, 257–259 (2008).
24. J. C. Goldschmidt, M. Peters, A. Bösch, H. Helmers, F. Dimroth, S. W. Glunz, and G. Willeke, "Increasing the efficiency of fluorescent concentrator systems," Sol. Energy Mater. Sol. Cells **93**, 176–182 (2009).
25. L. Desmet, A. J. Ras, D. K. de Boer, and M. G. Debije, "Monocrystalline silicon photovoltaic luminescent solar concentrator with 4.2% power conversion efficiency," Opt. Lett. **37**, 3087–3089 (2012).
26. F. Mateen, H. Oh, J. Kang, S. Y. Lee, and S.-K. Hong, "Improvement in the performance of luminescent solar concentrator using array of cylindrical optical fibers," Renew. Energy **138**, 691–696 (2019).
27. F. Mateen, M. Ali, S. Y. Lee, S. H. Jeong, M. J. Ko, and S.-K. Hong, "Tandem structured luminescent solar concentrator based on inorganic carbon quantum dots and organic dyes," Sol. Energy **190**, 488–494 (2019).
28. F. Mateen, S. Y. Lee, and S.-K. Hong, "Luminescent solar concentrators based on thermally activated delayed fluorescence dyes," J. Mater. Chem. A **8**, 3708–3716 (2020).
29. C. S. Erickson, L. R. Bradshaw, S. McDowall, J. D. Gilbertson, D. R. Gamelin, and D. L. Patrick, "Zero-reabsorption doped-nanocrystal luminescent solar concentrators," ACS nano **8**, 3461–3467 (2014).

30. I. Coropceanu and M. G. Bawendi, "Core/shell quantum dot based luminescent solar concentrators with reduced reabsorption and enhanced efficiency," Nano Lett. **14**, 4097–4101 (2014).
31. C. Li, W. Chen, D. Wu, D. Quan, Z. Zhou, J. Hao, J. Qin, Y. Li, Z. He, and K. Wang, "Large stokes shift and high efficiency luminescent solar concentrator incorporated with $CuInS_2$/ZnS quantum dots," Sci. Rep. **5**, 17777 (2015).
32. W. G. J. H. M. van Sark, K. W. J. Barnham, L. H. Slooff, A. J. Chatten, A. Büchtemann, A. Meyer, S. J. McCormack, R. Koole, D. J. Farrell, R. Bose, E. E. Bende, A. R. Burgers, T. Budel, J. Quilitz, M. Kennedy, T. Meyer, C. D. M. Donegá, A. Meijerink, and D. Vanmaekelbergh, "Luminescent solar concentrators—a review of recent results," Opt. Express **16**, 21773–21792 (2008).
33. J. Bomm, A. Büchtemann, A. J. Chatten, R. Bose, D. J. Farrell, N. L. A. Chan, Y. Xiao, L. H. Slooff, T. Meyer, A. Meyer, W. G. J. H. M. van Sark, and R. Koole, "Fabrication and full characterization of state-of-the-art quantum dot luminescent solar concentrators," Sol. Energy Mater. Sol. Cells **95**, 2087–2094 (2011).
34. X. Wang, T. Wang, X. Tian, L. Wang, W. Wu, Y. Luo, and Q. Zhang, "Europium complex doped luminescent solar concentrators with extended absorption range from UV to visible region," Sol. Energy **85**, 2179–2184 (2011).
35. Y. Zhao and R. R. Lunt, "Transparent luminescent solar concentrators for large-area solar windows enabled by massive Stokes-shift nanocluster phosphors," Adv. Energy. Mater. **3**, 1143–1148 (2013).
36. Y. Zhao, G. A. Meek, B. G. Levine, and R. R. Lunt, "Near-infrared harvesting transparent luminescent solar concentrators," Adv. Opt. Mater. **2**, 606–611 (2014).
37. M. Pravettoni, C. S. P. Lòpez, and R. P. Kenny, "Impact of the edges of a backside diffusive reflector on the external quantum efficiency of luminescent solar concentrators: experimental and computational approach," Am. J. Eng. Appl. Sci. **9**, 53–63 (2016).
38. Y. Li, Y. Sun, and Y. Zhang, "Regional measurements to analyze large-area luminescent solar concentrators," Renew. Energy **160**, 127–135 (2020).
39. Y. Li, J. Olsen, K. Nunez-Ortega, and W.-J. Dong, "A structurally modified perylene dye for efficient luminescent solar concentrators," Sol. Energy **136**, 668–674 (2016).
40. Y. Li, Y. Sun, Y. Zhang, and W.-J. Dong, "Improving the photostability of printed organic photovoltaics through luminescent solar concentrators," Opt. Mater. **108**, 110194 (2020).
41. Y. Li, Y. Sun, and Y. Zhang, "Boosting the cost-effectiveness of luminescent solar concentrators through subwavelength sanding treatment," Sol. Energy **198**, 151–159 (2020).
42. E. F. Zalewski and J. Geist, "Solar cell spectral response characterization," Appl. Opt. **18**, 3942–3947 (1979).
43. D. Sahin, B. Ilan, and D. F. Kelley, "Monte-Carlo simulations of light propagation in luminescent solar concentrators based on semiconductor nanoparticles," J. Appl. Phys. **110**, 033108 (2011).
44. S. W. Leow, C. Corrado, M. Osborn, M. Isaacson, G. Alers, and S. A. Carter, "Analyzing luminescent solar concentrators with front-facing photovoltaic cells using weighted Monte Carlo ray tracing," J. Appl. Phys. **113**, 214510 (2013).
45. J. P. Shu, X. W. Zhang, P. J. Wang, R. W. Chen, H. H. Zhang, D. K. Li, P. Zhang, and J. Xu, "Monte-Carlo simulations of optical efficiency in luminescent solar concentrators based on all-inorganic perovskite quantum dots," Physica B **548**, 53–57 (2018).
46. M. A. Green, E. D. Dunlop, J. Hohl-Ebinger, M. Yoshita, N. Kopidakis, and X. Hao, "Solar cell efficiency tables (version 56)," Prog. Photovolt. **28**, 629–638 (2020).